Mechanically manipulating glymphatic transport by ultrasound combined with microbubbles

Dezhuang Ye[a,1], Si Chen[a,1], Yajie Liu[a], Charlotte Weixel[a] 🅘, Zhongtao Hu[a], Jinyun Yuan[a], and Hong Chen[a,b,c,d,2] 🅘

The glymphatic system is a perivascular fluid transport system for waste clearance. Glymphatic transport is believed to be driven by the perivascular pumping effect created by the pulsation of the arterial wall caused by the cardiac cycle. Ultrasound sonication of circulating microbubbles (MBs) in the cerebral vasculature induces volumetric expansion and contraction of MBs that push and pull on the vessel wall to generate a MB pumping effect. The objective of this study was to evaluate whether glymphatic transport can be mechanically manipulated by focused ultrasound (FUS) sonication of MBs. The glymphatic pathway in intact mouse brains was studied using intranasal administration of fluorescently labeled albumin as fluid tracers, followed by FUS sonication at a deep brain target (thalamus) in the presence of intravenously injected MBs. Intracisternal magna injection, the conventional technique used in studying glymphatic transport, was employed to provide a comparative reference. Three-dimensional confocal microscopy imaging of optically cleared brain tissue revealed that FUS sonication enhanced the transport of fluorescently labeled albumin tracer in the perivascular space (PVS) along microvessels, primarily the arterioles. We also obtained evidence of FUS-enhanced penetration of the albumin tracer from the PVS into the interstitial space. This study revealed that ultrasound combined with circulating MBs could mechanically enhance glymphatic transport in the brain.

glymphatic | focused ultrasound | mechanics | intranasal | cerebral blood vessels

The glymphatic system is a glial-dependent perivascular network in the brain that functions in waste clearance and is analogous to the lymphatic system in the peripheral organs (1, 2). The glymphatic system was characterized for the first time in 2012 by Iliff et al. (3). Iliff et al. showed that fluorescent tracers injected into the cerebral spinal fluid (CSF) through intracisternal magna injections (ICM) entered the brain along cortical-penetrating arterioles through the perivascular space (PVS) that was fully enwrapped by astrocytic endfeet. Their subsequent studies suggested that fluorescent tracers passed into the brain interstitium, moved toward the venous PVS, and ultimately moved into the cervical lymphatic system. The currently widely accepted mechanism for glymphatic transport proposes that glymphatic influx into and through the brain is driven, at least in part, by the perivascular pumping effect generated by arterial wall pulsation induced by the cardiac cycle (4). Indeed, carotid artery ligation significantly reduced arterial pulsatility and slowed the rate of perivascular exchange in the brain (5). Systemic administration of the adrenergic agonist dobutamine increased the pulsatility of penetrating arteries and enhanced CSF penetration into the parenchyma compared with the control (6). By contrast, angiotensin-II treatment induces hypertension and reduces the velocity of CSF flow (7).

The glymphatic system removes brain metabolic wastes such as excess proteins and harmful metabolites in the interstitial space. The discovery of the glymphatic pathway provides new insights into how waste clearance works in the healthy brain, why we need to sleep, and the importance of efficient waste clearance in healthy aging (8). Impaired glymphatic transport is implicated in multiple neurological diseases, such as neurodegenerative diseases, traumatic brain injury, and stroke (8–14). Enhanced glymphatic transport may mitigate brain diseases caused by impaired glymphatic clearance, and several strategies have been proposed to enhance glymphatic function. For example, mannitol treatment in mice led to plasma hyperosmolarity and a nearly fivefold increase in CSF influx (15). Dietary supplements, such as omega-3 polyunsaturated fatty acids, promoted amyloid-β clearance in mice by promoting aquaporin-4-dependent glymphatic transport (16, 17). Nonpharmacologic methods, such as sleep and physical exercise, have also been reported to up-regulate glymphatic flow (18–20).

We postulated that glymphatic transport could be mechanically enhanced by ultrasound. Ultrasound, a noninvasive tool to generate mechanical effects, can penetrate the scalp and skull and reach the entire brain in animals and humans (21). Focused ultrasound (FUS), which concentrates ultrasound energy into a defined focal region, can target a

specific brain area with millimeter precision (22, 23). Effects from the FUS can be amplified at the targeted cerebral vasculature and surrounding brain tissue when combined with microbubbles (MBs) (24). MBs—compressible gas bubbles with a size comparable to red blood cells—were introduced in the clinic almost three decades ago as ultrasound contrast agents for imaging blood circulation (25). After intravenous (IV) injection, MBs are confined in the vasculature and circulate in the bloodstream like red blood cells. Ultrasound sonication leads to volumetric expansion and contraction of these compressible MBs, and these volumetric oscillations generate mechanical forces that push and pull on the adjacent vessel wall, thereby inducing vessel dilation and invagination (26). Vessel pulsation induced by FUS-activated MBs (FUSMB) may generate the MB pumping effect.

Our previous studies reported that FUSMB enhanced the penetration and accumulation of intranasally (IN) administered agents in the brain (27–32). IN-administered agents reach the brain through the olfactory and trigeminal nerve pathways (33). Once these agents reach the brain entry points, the perivascular pumping effect distributes them throughout the brain along the cerebral PVS (34, 35). Previous studies used invasive routes to study the glymphatic system (e.g., intraventricular infusion or ICM injection) (3). By contrast, intranasal administration provides a novel, noninvasive route to investigate the glymphatic pathway in intact brains. Our previous studies reported that FUSMB enhanced the accumulation of IN-administered agents in the targeted mouse brain region (27–32). Those studies primarily focused on drug delivery outcomes, including increased drug accumulation in the brain and cellular uptake after FUSMB. However, the biophysical mechanism of FUSMB-mediated agent transport in the brain remains unclear, particularly with respect to direct evidence regarding the spatial distribution of agents in the glymphatic system.

The objective of this study was to evaluate whether FUSMB could mechanically enhance glymphatic transport. Fluorescently labeled albumin was IN administered to anesthetized mice, followed by FUS sonication of the mouse brain in the presence of IV-injected MBs. As a comparative reference, we performed FUSMB treatment in additional mice injected with the same agents through the established ICM route to the glymphatic system. Fluorescence imaging of the labeled tracer in optically cleared ex vivo brain tissue revealed that FUSMB enhanced glymphatic transport in the brain.

Results

FUSMB Enhanced Albumin Transport to the Targeted Brain Region.
We applied FUS on one side of the thalamus after IN administration of fluorescently labeled albumin (Fig. 1A). Mice were killed 15 min after sonication. Mouse brains were harvested, sectioned into 1-mm thick coronal slices, imaged at low magnification to capture the tracer distribution in the whole slices, and then optically cleared for confocal fluorescence imaging (SI Appendix, Fig. S1). The low-magnification fluorescence images show that FUSMB enhanced albumin tracer accumulation within the FUS-sonicated brain region (FUS+) compared with the contralateral nonsonicated region (FUS–), as shown in Fig. 1B. The insets in Fig. 1B display confocal fluorescence images taken at a higher magnification after tissue clearance. The higher-magnification images confirmed that IN administration without FUS led to the distribution of the tracer in the PVS; however, the tracer concentration was low. In contrast, FUS sonication enhanced tracer transport in the perivascular and extracellular space. Quantification of the fluorescence intensity of the brain slices found that FUSMB enhanced the accumulation of albumin

by 1.49-fold on average compared with the contralateral FUS-side (Fig. 1C, P < 0.01). These results revealed that ultrasound combined with MBs enhanced the transport of IN-administered tracer within the sonicated brain region.

To confirm that it was the combination of FUS and MBs that led to the enhanced tracer transport, we included three control groups: (1) IN administration of the albumin tracer without FUS and MBs (FUS– MB–), (2) IN administration of the albumin tracer with FUS but without MBs (FUS+ MB–), and (3) IN administration of the albumin tracer with MBs but without FUS (FUS– MB+). All mice in these control groups showed low tracer accumulation (SI Appendix, Fig. S2) similar to that observed in Fig. 1B at the FUS– side. Findings from these control groups verified that the enhanced tracer transport was achieved by ultrasound combined with MBs.

To determine whether the enhancement effect of FUSMB is limited to IN-administered agents, we conducted FUSMB treatment following tracer injection through the ICM route (Fig. 1A). ICM-injected tracers are known to utilize the perivascular pathway for transport within the brain and are commonly used in studies of the glymphatic system (36, 37). Similar to the findings presented in Fig. 1 B and C, we observed that FUSMB enhanced the transport of ICM-injected tracers at the FUS-targeted brain site by 1.74-fold compared to the contralateral side (Fig. 1 D and E, P < 0.01). These findings suggested that FUSMB can enhance glymphatic transport for both IN- and ICM-administered agents.

FUSMB Enhanced Albumin Transport via the PVS.
To investigate the microscopic distribution of IN-administered albumin following FUSMB, we stained the optically cleared brain slices with lectin, a protein that binds to vessel walls, and antiglial fibrillary acidic protein (GFAP) antibody, which identifies astrocytes. We found that albumin accumulated in the PVS between the vessel wall and astrocytic endfeet in the FUS-targeted brain region. This was consistently observed in both large (Fig. 2A and Movie S1) and small (Fig. 2C and Movie S2) vessels. By contrast, little to no albumin tracer was observed in the PVS on the contralateral FUS-side of the brain (Fig. 2 B and D). Cross-section images of the blood vessel confirmed that albumin is predominantly located in the PVS (Fig. 2 E and F and Movie S3).

FUSMB Enhanced Albumin Transport Primarily via Arterioles.
To further investigate types of vessels that facilitate FUSMB-enhanced albumin transport, we stained the optically cleared brain slices with antismooth muscle actin (αSMA) antibody and lectin to differentiate arterioles, capillaries, and venules. We performed FUSMB on one side of the brain in two groups of mice (n = 6 per group) after IN and ICM administration of the tracer, respectively. One mouse from the IN delivery group was excluded from the analysis because the αSMA staining did not work well. Three-dimensional (3D) confocal microscopy imaging of the FUSMB-treated brain region further verified that FUSMB significantly enhanced the transport of albumin tracers in the FUS-targeted brain region (Figs. 3A and 4A and Movies S4 and S5) compared with the contralateral nontreated brain region (Figs. 3B and 4B). We observed that albumin in the FUS+ region was distributed primarily along the PVS of αSMA-positive vessels (Figs. 3A and 4A and Movies S4 and S5). To quantify the distribution of albumin along different types of vessels, we first computationally segmented individual vessels based on the lectin staining. Vessels ranging from 40 μm to 200 μm in length were selected for the quantification. For each selected vessel, we measured the lumen diameter to identify arterioles, venules, and capillaries based on the αSMA staining and vessel diameters (38, 39). We quantified albumin
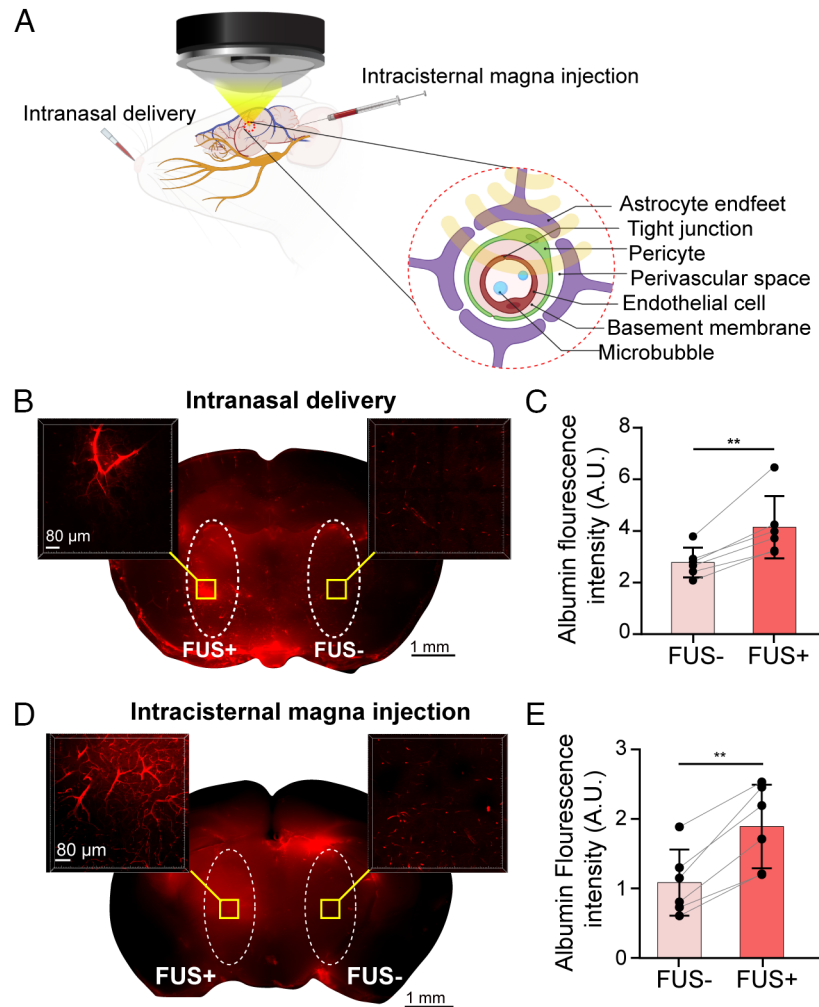
Fig. 1. FUSMB enhanced glymphatic albumin tracer transport to the targeted brain region. (A) Illustration of the experimental method. Intranasal delivery (IN) or intracisternal magna injection (ICM) of fluorescently labeled albumin was followed by FUS sonication of a targeted brain region (left thalamus) after injection of MBs through the tail vein. (B) Representative low magnification (2×) fluorescent image of IN-administered albumin tracer in a 1-mm thick brain section before tissue clearance (*Middle*), and regional distribution of the tracer at high magnification (10×) in the FUS-treated (*Left*) and contralateral nontreated sides (*Right*) after tissue clearance. (C) The fluorescence intensity of the IN-administered albumin tracer in the FUS-treated side (FUS+) was significantly higher than that in the contralateral nontreated control side (FUS−) with n = 6. (D) Representative low magnification (2×) fluorescent images of ICM-delivered albumin tracer in a 1-mm thick brain section before tissue clearance (*Middle*), and regional distribution of the tracer at high magnification (10×) in the FUS-treated (*Left*) and contralateral nontreated sides (*Right*) after tissue clearance. (E) The fluorescence intensity of the ICM-delivered albumin tracer in the FUS-treated side (FUS+) was significantly higher than that in the contralateral nontreated control side (FUS−) with n = 6. The fluorescence intensity was measured within the region of interest (ROI) defined by the white dashed line in the low-magnification brain images prior to tissue clearance. **$P < 0.01$

concentration by integrating the average albumin fluorescence intensity within 10 μm from the vessel's surface (*SI Appendix,* Fig. S1*C*). To compare among different animals, we calculated the mean albumin fluorescence intensities for each of the three vessel types in each animal (Figs. 3*C* and 4*C*).

Regardless of whether tracers were delivered via the IN or ICM route, FUSMB consistently improved glymphatic transport. For comparison among different animals, the average albumin fluorescence intensity around arterioles in the FUSMB-treated brain region was increased by 8.75-fold in the IN group (Fig. 3*C*, $P < 0.05$) and 3.49-fold in the ICM group (Fig. 4*C*, $P < 0.01$) when compared to the contralateral nontreated side. Comparing individual arterioles in the FUS+ side versus the FUS− side, FUSMB increased the albumin fluorescence intensity by 9.09-fold and 3.38-fold for both IN and ICM groups, respectively (Figs. 3*D* and 4, $P < 0.0001$). For capillaries, the enhancement was 5.86-fold (Fig. 3*C*, $P < 0.05$) and 2.16-fold (Fig. 4*C*, $P < 0.05$) when comparing among different animals and 5.99-fold and 2.24-fold when comparing among vessels (Figs. 3*D* and 4*D*, $P < 0.0001$) for IN and ICM groups, respectively. For venules, we did not observe a

significant difference in the average albumin fluorescence intensity between FUS+ and FUS− sides when comparing among different mice from the IN group (Fig. 3*C*). However, a significant difference was identified among mice from the ICM group, where the FUS+ side exhibited a 2.21-fold increase in fluorescence intensity (Fig. 4*C*, $P < 0.05$). Significant differences were observed between the FUS+ and FUS− sides when examining individual venules in both IN and ICM groups. FUS increased the albumin intensity along venules by 7.06-fold for IN delivery (Fig. 3*D*, $P < 0.05$) and 2.33-fold for ICM delivery (Fig. 4*D*, $P < 0.0001$). By comparing albumin intensity among these three vessel types in the FUSMB-treated brain region, we found that the albumin fluorescence intensity was higher along arterioles than that of capillaries and venules.

FUSMB Enhanced Albumin Transport into the Brain Interstitial Space. Confocal microscopy imaging also revealed that FUSMB enabled the extravasation of albumin from the PVS into the interstitial space (Fig. 5 *A* and *C* and Movies S6 and S7). In contrast, only a little albumin tracer was found in the interstitial space on the contralateral nontreated side of the brain (Fig. 5 *B*
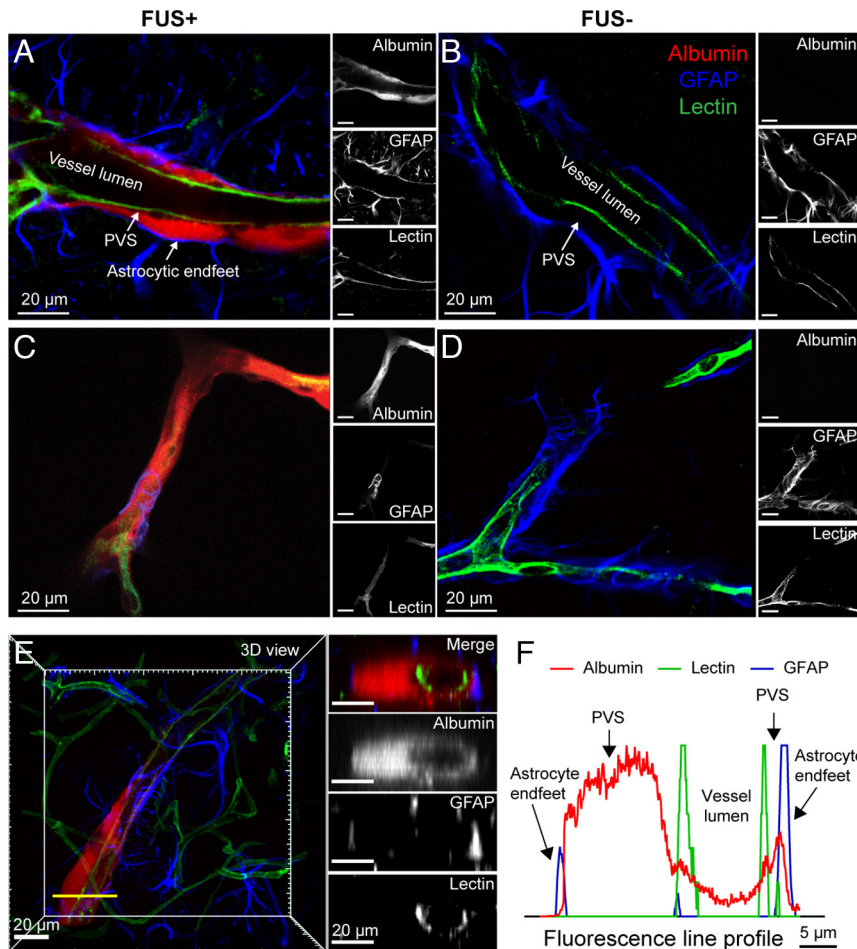
Fig. 2. FUSMB enhanced IN-administered albumin transport along the PVS. (*A*) and (*B*) are representative confocal microscopy images of a relatively large blood vessel in the FUS+ and FUS- site, respectively. (*C*) and (*D*) are representative confocal microscopy images of a relatively small blood vessel in the FUS+ and FUS- site, respectively. Fluorescently labeled albumin (red) was observed in the PVS, defined as the space between the lectin-stained vessel wall and the GFAP-labeled astrocyte endfeet of cerebral blood vessels, in the FUS+ brain region. Little to no albumin tracer was observed in the contralateral nontreated (FUS-) brain regions. (*A–D*) For each panel, the image on the left is a merged image of three channels (red, albumin; green, lectin; blue, GFAP) and the three images on the right are those obtained from individual images for albumin, GFAP, and lectin, respectively. (*E*) and (*F*) are representative cross-section images and the corresponding fluorescence profile, which verified that albumin was transported along the PVS. Images on the *Right* panel of (*E*) show the cross-section images of a vessel captured along the yellow transect line in the 3D image shown on the *Left*. The top image displays the merged image of three channels (red, albumin; green, lectin; blue, GFAP). The three images below show the individual images for albumin, GFAP, and lectin, respectively. (Scale bars, 20 µm) (*F*) The fluorescence profile along the yellow transect line indicates that albumin accumulates in the PVS between the vessel wall and the astrocytic endfeet.

and *D*). We observed that albumin extravasated from the PVS of both arterioles (*SI Appendix*, Fig. S3*A* and Movie S8) and capillaries (*SI Appendix*, Fig. S3*B* and Movie S9) and penetrated into the brain interstitial space.

Discussion

The glymphatic system is a newly discovered brain fluid transportation system. This discovery presents enormous opportunities to develop strategies to investigate brain fluid dynamics and to treat brain diseases caused by impaired glymphatic transport. Our study proposes that FUS combined with MBs can be used to mechanically manipulate glymphatic transport in targeted brain regions. This enhanced transport is primarily through the PVS of arterioles.

Our study obtained the direct evidence that FUSMB enhanced the transport of a fluorescently labeled protein tracer in the PVS. Previously, Meng et al. observed that the MRI contrast agent accumulated in the draining veins and subarachnoid spaces following FUSMB in human brains (40). Lee et al. demonstrated that FUSMB enhanced soluble Aβ clearance from the brain to the CSF using a cervical lymph node ligation model in mice (41). These studies suggest that FUSMB may be used to study

and manipulate the glymphatic system; however, the evidence presented did not show a direct effect of FUSMB on the glymphatic system. By contrast, our study using confocal microscopy imaging obtained direct evidence that unequivocally proved that FUSMB enhanced the glymphatic transport of a labeled protein agent in mice.

Our results show that FUSMB enhanced glymphatic transport primarily along arterioles. The perivascular pumping effect generated by arterial wall pulsation has been considered the dominant driving force for glymphatic transport into and throughout the brain. A previous study by Iliff et al. (3) reported that ICM-injected tracers rapidly entered the brain along cortical surface arteries and penetrating arterioles. The tracer was not observed around veins at early time points (< 10 min after injection). Similarly, our data show that FUSMB-enhanced albumin tracer accumulation occurred primarily along arterioles, followed by capillaries and venules. IV-injected MBs circulate in the whole vascular network, including arterioles, venules, and capillaries. Our previous ultra-high-speed photomicrographic imaging of MB interactions with microvessels observed that FUS sonication–induced MB expansion and contraction generated pulsation-like behavior in arterioles, venules, and capillaries (42, 43). Thus, MB-induced
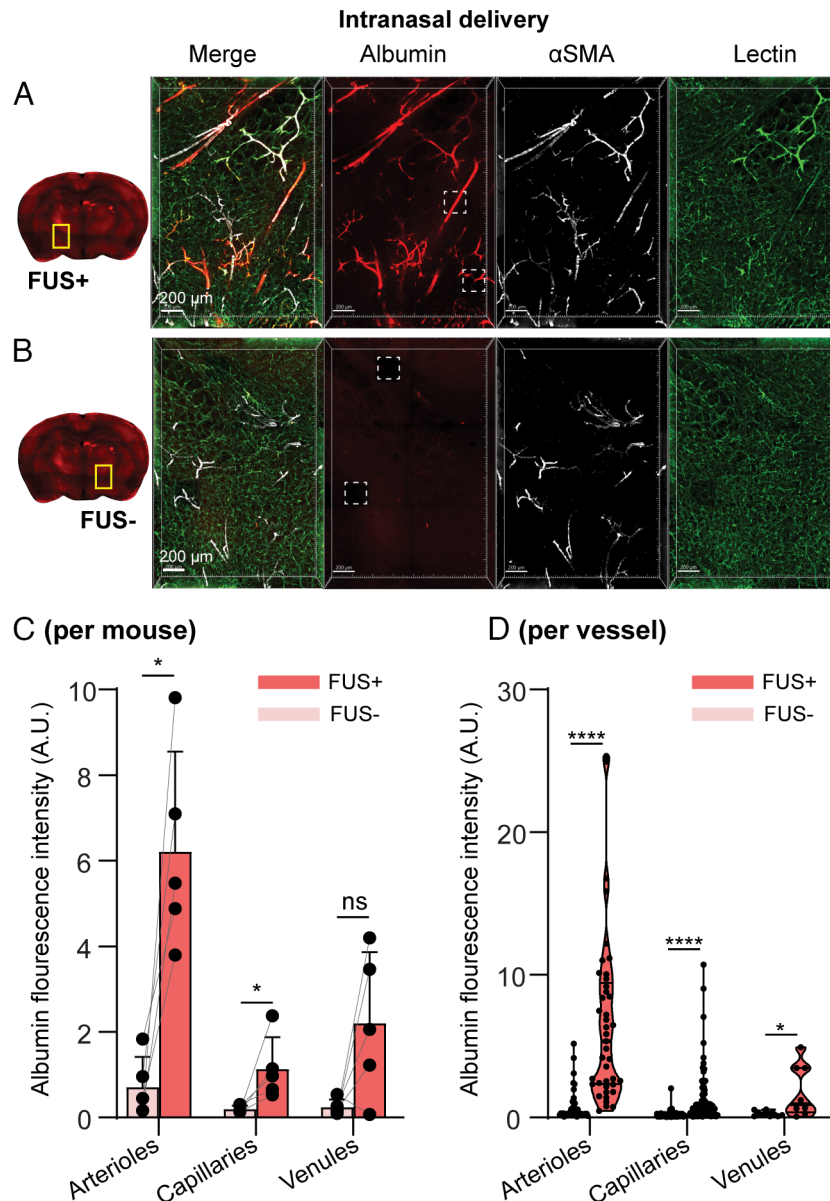
Fig. 3. FUSMB enhanced the transport of intranasal (IN)-administered albumin primarily along arterioles. 3D confocal microscopy images (5×) were captured within a volume of 1.52 × 2.24 × 0.26 mm³ in (*A*) the FUS-treated brain region (FUS+, yellow box) and (*B*) the contralateral nontreated brain region (FUS−, yellow box). For each panel, the image on the left is a merged image of three channels (red, albumin; green, lectin; white, αSMA), and the three images on the right display those obtained from individual channels. (*C*) Average albumin fluorescence intensity for each mouse along arterioles (*Left*), capillaries (*Middle*), and venules (*Right*), in FUS-treated brain region (FUS+) and the contralateral nontreated (FUS−) brain (n = 5). (*D*) Albumin fluorescence intensity along individual arterioles (*Left*), capillaries (*Middle*), and venules (*Right*) in the FUS+ and FUS− regions of all mice (arteriole FUS− n = 46, FUS+ n = 41; capillary FUS− n = 133, FUS+ n=116; venule FUS− n = 10, FUS+ n = 8). Arteriole: αSMA+, vessel lumen diameter 6 to 30 μm; capillary: vessel lumen diameter 1 to 6 μm; venule: αSMA−, vessel lumen diameter 6 to 30 μm. *$P < 0.05$, ****$P < 0.0001$. The stack size for single-vessel quantification was 200 × 200 × 28 μm³ captured with a 20× objective and a voxel size of 0.1 × 0.1 × 0.87 μm³. It is noted that these 5× images shown in *A* and *B* were captured after imaging with the 20× objective. During the 20× imaging process, fluorescence bleaching occurred, resulting in the dark square regions highlighted by white dashed boxes in *A* and *B*. The remaining images were not affected by the photobleaching effect.

vessel pulsation generates a MB pumping effect that may drive fluid transport along the PVS, regardless of vessel type. The observed tracer distribution primarily in the PVS of arterioles supports the previous observation that glymphatic transport was driven by periarteriole bulk flow and reveals that FUSMB enhanced the bulk flow. Confocal microscopy imaging of optically cleared tissue provided 3D high-resolution images to reveal the spatial distribution of the tracer in the glymphatic system along the vessels. However, this ex vivo imaging approach required transcardial perfusion of the mice to fix the brain tissue and optical clearance of the tissue, which could collapse the PVS and artificially mislocate the tracers (7). Our study compared the

FUSMB-treated side and the contralateral nontreated side of the same brain, which underwent the same postprocessing procedure, including tissue fixation and clearance under the same condition. Future studies can be performed using in vivo two-photon microscopy to reveal the dynamics of agent transport and avoid any potential artifacts associated with ex vivo tissue preparation.

Moreover, our findings showed that FUSMB enhanced the penetration of albumin from the PVS to the interstitial space. This is consistent with our previous reports that FUSMB increased the accumulation of IN-administered agents (e.g., brain-derived neurotrophic factor, immune checkpoint inhibitor, gold nanoparticles, and adeno-associated viral vectors) in the
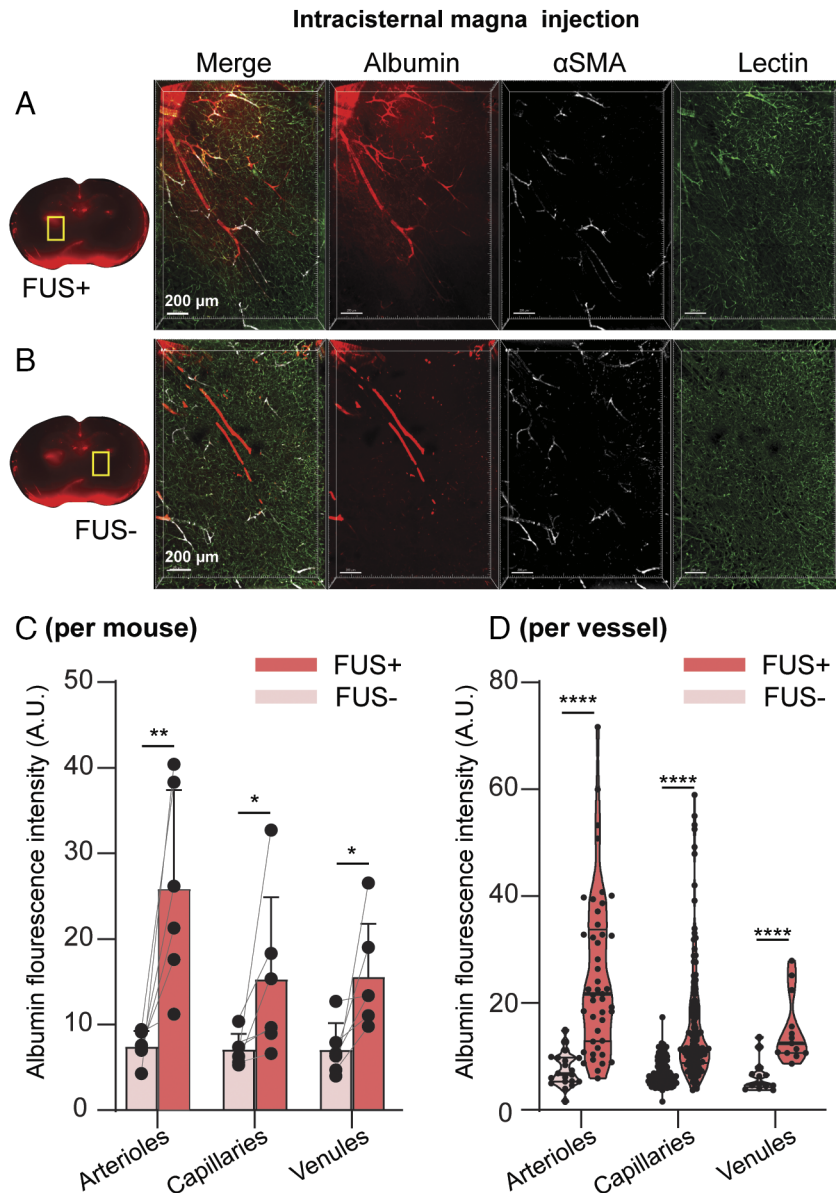
Fig. 4. FUSMB enhanced the transport of intracisternal magna (ICM)-injected albumin primarily along arterioles. 3D confocal microscopy images (5×) were captured within a volume of 1.52 × 2.24 × 0.26 mm^3 in (*A*) the FUS-treated brain region (FUS+, yellow box) and (*B*) the contralateral nontreated brain region (FUS−, yellow box). For each panel, the image on the left is a merged image of three channels (red, albumin; green, lectin; white, αSMA), and the three images on the right display those obtained from individual channels. (*C*) Average albumin fluorescence intensity for each mouse along arterioles (*Left*), capillaries (*Middle*), and venules (*Right*) in FUS-treated brain region (FUS+) and the contralateral nontreated (FUS−) brain (n = 6). (*D*) Albumin fluorescence intensity along individual arterioles (*Left*), capillaries (*Middle*), and venuels (*Right*) in the FUS+ and FUS− regions of all mice (arteriole FUS− n = 20, FUS+ n = 46; capillary FUS− n = 167, FUS+ n = 126; venule FUS− n = 13, FUS+ n = 13). Arteriole: αSMA+, vessel lumen diameter 6 to 30 μm; capillary: vessel lumen diameter 1 to 6 μm; venule: αSMA−, vessel lumen diameter 6 to 30 μm. *$P < 0.05$, **$P < 0.01$, ****$P < 0.0001$.

FUS-treated brain region (28–32). Our previous ultra-high-speed photomicrographic imaging indicated that MB oscillations push and pull on the adjacent vessel wall and the surrounding connective tissue (42). MB oscillations may generate a convection flow between the PVS and the interstitial space, enabling efficient transport and exchange of substances between these two spaces. Thus, we suspect that the MB pumping effect contributed to agent transport along the PVS and penetration from the PVS to the interstitial space. It is worth noting that we observed cellular uptake of albumin via glymphatic delivery in some of our recorded images. Although the investigation of cellular uptake of albumin was not the primary objective of the current study, it is interesting to conduct future research to determine the mechanism of brain parenchymal cell uptake of therapeutic agents

delivered by FUSMB-mediated glymphatic transport. These investigations will help to advance this approach for the pharmacological treatment of brain disease.

The noninvasive IN route for investigating glymphatic transport has the potential to be utilized in the study of glymphatic function in humans, which is currently limited by the absence of noninvasive approaches to access the glymphatic system. The most commonly used method for studying the glymphatic system is the ICM injection (3), which is known to utilize the perivascular pathway for transport within the brain (36, 37). Our results demonstrate that tracers delivered by IN also use the PVS for transport in the brain. The FUSMB-enhanced transport effect of IN-administered tracers is comparable to that of ICM-injected tracers. These findings suggest that IN delivery can be used as a noninvasive approach to studying
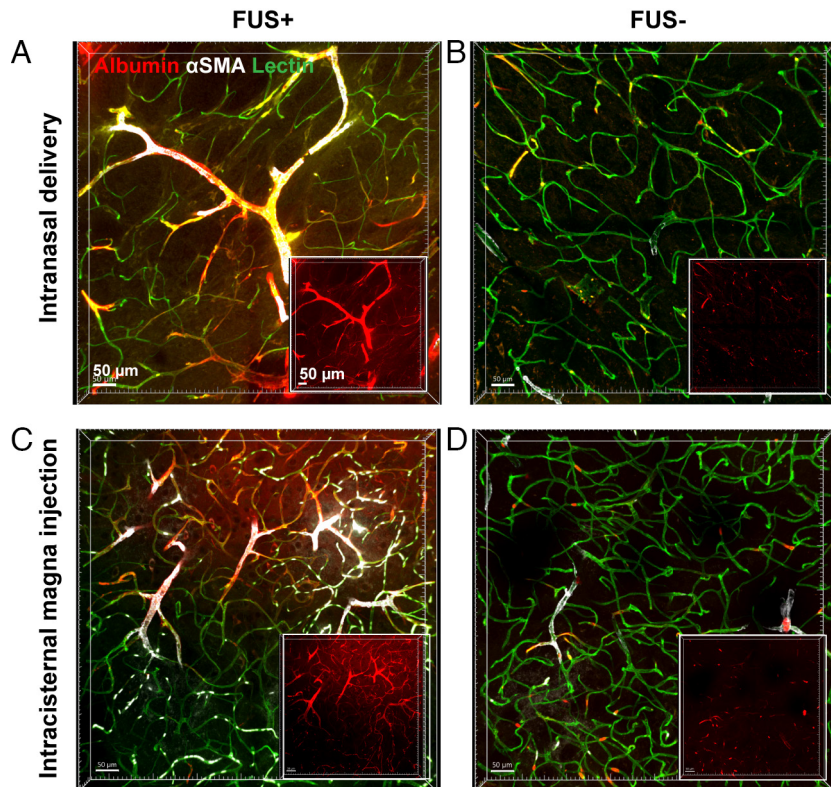
Fig. 5. FUSMB enhanced albumin transport into the interstitial space. Albumin (red) extravasation from the PVS into the interstitial space was observed in arterioles and capillaries in the FUS-treated brain region (FUS+). The *Insets* are the albumin channel. (Scale bars, 50 μm.) *A* and *B* are representative fluorescence images from the IN group at FUS-treated sites (*A*) and the contralateral side (*B*), respectively. (*C*) and (*D*) are representative images from the ICM group at FUS-treated sites and the contralateral side, respectively.

the glymphatic system, opening the door to developing clinical techniques for assessing glymphatic function. However, it should be noted that disease conditions in the nasal cavity, such as upper respiratory tract infections, may impact IN delivery to the brain, and these factors should be carefully considered when applying this method for glymphatic research (44).

The FUSMB treatment parameters used in this study were similar to those used to induce transient blood–brain barrier (BBB) opening (45). However, the enhanced transport of albumin following IN administration was not a result of trans-BBB leakage from the blood because the amount of albumin that entered the blood circulation was not significantly different from that of the control without injecting albumin (*SI Appendix*, Fig. S4). In addition, IV-injected albumin displayed a discontinuous distribution along the vessel wall (*SI Appendix,* Figs. S5 and S6 and Movies S10 and S11, magenta), possibly due to transcytosis, as previously suggested (46). Conversely, IN-delivered albumin exhibited a continuous distribution along the vessels (*SI Appendix*, Figs. S5*A* and S6*A* and Movie S10, red), similar to ICM injection (*SI Appendix,* Figs. S5*B* and S6*B* and Movie S11, red). These observations further confirm that the enhanced transport of albumin after IN delivery is not a result of trans-BBB leakage, but rather due to glymphatic transport. It is interesting to assess whether the FUSMB technique can enhance glymphatic transport without BBB opening in the future. It is also interesting to investigate whether agents in the PVS can be transported into the blood through the opened BBB, which may enable the clearance of brain waste through blood circulation. Future studies are also warranted to determine the impact of different FUS parameters on glymphatic transport to establish the efficacy profiles of FUSMB in glymphatic manipulation.

This study has several limitations. First, mice were killed shortly (15 min) after FUS sonication to capture the direct effect of FUSMB on glymphatic transport. Previous studies reported increased astrocyte reactivity and microglia activation between 3 and 48 h after FUSMB, which resolved over a period of days (46, 47). These delayed biological effects may contribute to glymphatic clearance (40), which is worth exploring in future work. Second, the anesthetic regimens play an important role in glymphatic transport (48, 49). Future studies also need to look into the FUSMB effects on the glymphatic system under different anesthetic regimens.

In conclusion, this study opens opportunities to use ultrasound combined with MBs as a noninvasive and nonpharmacological approach to manipulate glymphatic transport. FUSMB has the promise to enhance waste clearance in the brain and potentially mitigate brain diseases caused by impairments in glymphatic system function.

Materials and Methods

Animals. All animal procedures were reviewed and approved by the Institutional Animal Care and Use Committee in accordance with the NIH guidelines for animal research (Institutional Animal Care and Use Committee protocol number 21-0187). NIH Swiss mice (6 to 8 wk, ~25 g body weight, female) were purchased from Charles River Laboratory. The animals were housed in a room maintained at 22 °C, 55% relative humidity, and a 12-h/12-h light/dark cycle with access to standard laboratory chow and water until the experiment. The mice were divided into five groups (n = 6 per group): 1) IN+FUSMB: IN administration of Alexa Fluor 555-conjugated bovine serum albumin tracer (BSA$_{A555}$) followed by FUSMB treatment; 2) IN only: IN administration of BSA$_{A555}$ without any treatment; 3) IN+FUS without MB: IN administration of BSA$_{A555}$ followed by FUS treatment without MB injection; 4) IN+MB without FUS: IN administration of BSA$_{A555}$ followed by MB injection without FUS treatment; and 5) ICM+FUSMB: ICM injection

of BSA_{A555} followed by FUSMB treatment. All mice were coinjected with Alexa Fluor 647-conjugated bovine serum albumin (BSA_{A647}) intravenously when IN or ICM delivery was completed.

Intranasal Administration. IN administration was performed as described previously (29). Briefly, mice were placed supine under anesthesia (1.5 to 2% v/v isoflurane in oxygen). The fluorescently labeled albumin was administered to the mouse nose using a micropipette tip (Fig. 1A). Three microliters of albumin solution was administered to each nostril of the mouse, alternating between the right and left nostrils every 2 min, for a total of eight times (12 μL per nostril, 24 μL in total). The total administration time was ~16 min. Following IN administration, the mice were moved to a customized stereotaxic-guided FUS device to receive sonication under anesthesia as described previously (22). The fur on the mouse's head was shaved to prepare for the FUSMB procedure.

Intracisternal Magna Injection. For ICM injection, mice were anesthetized (1.5 to 2% v/v isoflurane in oxygen) with their heads secured in a stereotaxic frame. The skin of the mouse's head and neck was shaved and cleaned with iodine and 70% ethanol. After making a skin incision, the muscle layers were retracted, and the cisterna magna was exposed. A volume of 5 μL of Alexa Fluor 555-conjugated bovine serum albumin was injected into the cisterna magna compartment at a speed of 2 μL/min using a Hamilton syringe fixed on a syringe pump. After injection, the needle was held for an additional 10 min to prevent backflow of CSF.

FUSMB Procedure. For the FUSMB procedure, ultrasound gel was applied to the exposed skin above the skull. A catheter was placed in the mouse tail vein for IV injection of MBs. A FUS transducer was positioned by the stereotaxic frame to target the left thalamus. Sonication started 30 min after the IN administration of the last drop of labeled albumin. Immediately before sonication, the mice were IV injected with a bolus of commercially available MBs (Definity®, Lantheus Medical Imaging) at a dose of 10 μL/kg. The FUS parameters used in this study were as follows: pressure = 0.4 MPa, central frequency = 1.5 MHz, pulse length = 6.7 ms, pulse repetition frequency = 5 Hz, sonication duration = 60 s.

Macroscopic Fluorescence Imaging. The anesthetized mouse was transcardially perfused 15 min after FUS sonication (or 45 min after the end of IN administration) using a perfusion pump at a speed of 5.5 mL/min. Lectin (Vector Laboratories) was injected through the tail vein before perfusion to label the blood vessel. The blood of the mouse was first washed away by a 60-mL perfusion solution containing 1×Phosphate-Buffered Saline (PBS), 10 U/mL heparin, and 0.5% w/v sodium nitrite (Sigma Aldrich). The mouse was then fixed by transcardial perfusion with a 50-mL fixation solution containing 1×PBS and 4% w/v paraformaldehyde (PFA) (Sigma Aldrich). Mouse brain was harvested and incubated in 4% PFA/PBS for 10 h at 4 °C. The fixed brain was sectioned as 1-mm thick coronal slices using a brain matrix (RBM-2000C; ASI Instruments, Inc.). The brain sections from all the groups were numbered and imaged using an Olympus MVX10 microscope with 2× objective (Olympus, Japan) before the clearance. Images were captured using a color camera (Olympus DP23) at ×0.63 magnification, and images were saved using MetaMorph software (Olympus). The fluorescence intensities of the brain slices were quantified using ImageJ (NIH) by calculating the average fluorescence intensity within the region of interest (ROI) on the left and the right sides of the brain thalamus. An elliptical shape with a short axis of ~1.6 mm and a long axis of ~10 mm was selected as the ROI for the fluorescence quantification, and the ROIs were marked on the left and right sides of the thalamus in Fig. 1. The analysis was carried out by experimenters who were unaware of the experimental groups, ensuring impartiality in the results.

Tissue Clearing. After macroscopic fluorescence imaging of the whole-brain slices, the brain slices from the FUSMB delivery group (groups 1 and 5) were transferred to a 24-well plate for tissue clearance. Tissue clearance was performed as described previously (50). Briefly, slices were incubated in ScaleS0 solution for 12 h to permeabilize the samples. Then, the slices were incubated in ScaleA2 solution for 36 h, followed by incubation in ScaleB4 solution for 24 h, and reincubated in ScaleA2 solution for 12 h. All incubations were performed at 37 °C in an incubator shaker at 75 rpm (New Brunswick Scientific). The samples were washed with 1×PBS at 4 °C for 6 h. ScaleS0, ScaleA2, ScaleB4, and ScaleS4 were prepared using a previously published protocol (50).

Immunofluorescence Staining. Cleared brain slices were stained with αSMA to identify arterioles or GFAP to identify astrocytes. In brief, AbScale solution, AbScale rinse solution, and ScaleS4 solution were prepared according to the previously published protocol (50). The primary antibody [αSMA (D4K9N, Cell Signaling Technology) or recombinant anti-GFAP antibody (Abcam, ab207165, Cambridge, MA, USA)] was diluted 1:150 in AbScale solution. Then, brain samples were incubated in AbScale solution containing the primary antibody for 36 h at 37 °C (with shaking). After incubation, the samples were washed twice in AbScale solution (2 h at room temperature with shaking) and then stained with the secondary antibody [Dylight 405 donkey anti-rabbit antibody (antibody: AbScale solution, 711475152, Jackson Laboratories, West Grove, PA, USA)] for 48 h. Then, the samples were washed with AbScale solution for 6 h and rinsed twice with AbScale rinse solution (2 h at room temperature with shaking). The samples were then refixed in 4% PFA/PBS for 1 h at room temperature with shaking and washed in 1×PBS for 1 h at room temperature with shaking. The samples were cleared in ScaleS4 solution for 12 h at 37 °C with shaking and stored in ScaleS4 at 4 °C until use for imaging.

3D Confocal Microscopy Imaging. Cleared and stained coronal brain sections were placed on a 35-mm glass-bottom dish (MatTek). Images were acquired using a Zeiss Celldiscoverer 7 (Carl Zeiss). For the fluorescently labeled albumin tracer, an excitation wavelength of 561 nm and an emission wavelength of 575 nm were used for the channel setting; for the SMA and GFAP, an excitation wavelength of 405 nm and an emission wavelength of 421 nm were used for the channel setting; and for the FITC-labeled lectin, an excitation wavelength of 488 nm and an emission wavelength of 520 nm were used for the channel setting. Images within a large field of view of the mouse thalamus region were captured in the FUS-treated region and the contralateral nontreated region of the brain section using a 5× or 10× objective. The PVS was visualized in the FUS-treated region and the contralateral nontreated region of the brain section by capturing using a 20× objective.

Single-Vessel Intensity Analysis. For each mouse brain, a total of five fields of view (each field of view's dimension was $200 \times 200 \times 28 \ \mu m^3$) were randomly selected from both the FUSMB-treated and nontreated contralateral thalamus region and were imaged using high-resolution confocal microscopy with 20× objective. The albumin intensity of ~6 to 7 vessels, within each field of view, was calculated. Single-vessel intensity analysis was performed using Imaris Version 9.8.0 (Oxford Instruments). The Zeiss Celldiscoverer 7 images captured using 20× objective were imported, 3D reconstructed, and processed using the Imaris Gaussian filter. Background subtraction was applied to the 488 nm (lectin) channel. Then, a 3D surface was constructed from the 488 nm (lectin) channel to encompass all vessels in the sample. The lectin channel was masked by the resulting surface so that all background noise outside the vessel region was eliminated before single-vessel surface reconstruction. Next, the surfaces of individual vessels, ranging in length from 40 μm to 200 μm, were computationally reconstructed. A surface was constructed to represent the spatial extent of each vessel based on lectin fluorescence. Albumin concentration was quantified by integrating the average albumin fluorescence intensity within 10 μm from the vessel's surface (*SI Appendix*, Fig. S1C). Vessel diameters were measured using the measurement function in Imaris. All the vessels were characterized as arterioles, capillaries, and venules by lectin+ αSMA+ staining and vessel diameters. A cutoff value of 6 μm was used to differentiate capillaries (38, 39) (arteriole: αSMA+, vessel lumen diameter 6 to 30 μm; capillary: vessel lumen diameter 1 to 6 μm; venule: αSMA−, vessel lumen diameter 6 to 30 μm). It is worth noting that a smaller number of venules (~2 to 3 per animal) were identified in each mouse brain compared to arterioles and capillaries (Figs. 3D and 4D). The single-vessel analysis was carried out by experimenters who were unaware of the experimental conditions.

Statistical Analysis. Statistical analysis was performed using GraphPad Prism (version 9.4.1, La Jolla, CA, USA). The normality test was first performed on all the data to determine the statistical test method. For brain slices prior to tissue clearance, differences in fluorescence intensity between the FUS+ and FUS- sites were determined using paired, two-tailed Student's t tests (Fig. 1 C and E). For single-vessel quantification comparisons, multiple paired t tests were used when comparing FUS+ and FUS− conditions between animals (Figs. 3C and 4C), and multiple Mann–Whitney U tests were used when comparing between vessels

(Figs. 3D and 4D). The upper/lower error bars depict the SD and the points represent individual data values. P-values < 0.05 were considered statistically significant.

Data, Materials, and Software Availability. All study data are included in the article and/or *supporting information*.

1. M. K. Rasmussen, H. Mestre, M. Nedergaard, Fluid transport in the brain. *Physiol. Rev.* **102**, 1025–1151 (2022).
2. H. Benveniste *et al.*, The glymphatic system and waste clearance with brain aging: A review. *Gerontology* **65**, 106–119 (2019).
3. J. J. Iliff *et al.*, A Paravascular pathway facilitates CSF flow through the brain parenchyma and the clearance of interstitial solutes, including amyloid β. *Sci. Transl. Med.* **4**, 147ra111 (2012).
4. N. A. Jessen, A. S. F. Munk, I. Lundgaard, M. Nedergaard, The glymphatic system–A beginner's guide. *Neurochem. Res.* **40**, 2583 (2015).
5. J. J. Iliff *et al.*, Cerebral arterial pulsation drives paravascular CSF–interstitial fluid exchange in the murine brain. *J. Neurosci.* **33**, 18190–18199 (2013).
6. I. F. Harrison *et al.*, Non-invasive imaging of CSF-mediated brain clearance pathways via assessment of perivascular fluid movement with diffusion tensor MRI. *Elife* **7**, 1–14 (2018).
7. H. Mestre *et al.*, Flow of cerebrospinal fluid is driven by arterial pulsations and is reduced in hypertension. *Nat. Commun.* **9**, 4878 (2018).
8. M. Nedergaard, S. A. Goldman, Glymphatic failure as a final common pathway to dementia. *Science* **370**, 50–56 (2020).
9. J. M. Tarasoff-Conway *et al.*, Clearance systems in the brain: Implications for Alzheimer disease. *Nat. Rev. Neurol.* **11**, 457–470 (2015).
10. I. F. Harrison *et al.*, Impaired glymphatic function and clearance of tau in an Alzheimer's disease model. *Brain* **143**, 2576–2593 (2020).
11. H. L. Chen *et al.*, Associations among cognitive functions, PIαSMA DNA, and diffusion tensor image along the perivascular space (DTI-ALPS) in patients with Parkinson's disease. *Oxid. Med. Cell. Longev.* **2021**, 1–10 (2021).
12. J. J. Iliff *et al.*, Impairment of glymphatic pathway function promotes tau pathology after traumatic brain injury. *J. Neurosci.* **34**, 16180–16193 (2014).
13. R. Goulay *et al.*, Subarachnoid hemorrhage severely impairs brain parenchymal cerebrospinal fluid circulation in nonhuman primate. *Stroke* **48**, 2301–2305 (2017).
14. E. V. Golanov *et al.*, Subarachnoid hemorrhage–Induced block of cerebrospinal fluid flow: Role of brain coagulation factor III (tissue factor). *J. Cereb. Blood Flow Metab.* **38**, 793 (2018).
15. B. A. Plog *et al.*, Transcranial optical imaging reveals a pathway for optimizing the delivery of immunotherapeutics to the brain. *JCI Insight* **3**, e120922 (2018).
16. H. Ren *et al.*, Omega-3 polyunsaturated fatty acids promote amyloid-β clearance from the brain through mediating the function of the glymphatic system. *FASEB J.* **31**, 282–293 (2017).
17. E. Zhang *et al.*, Omega-3 polyunsaturated fatty acids alleviate traumatic brain injury by regulating the glymphatic pathway in mice. *Front. Neurol.* **11**, 707 (2020).
18. D. Liu *et al.*, Continuous theta burst stimulation facilitates the clearance efficiency of the glymphatic pathway in a mouse model of sleep deprivation. *Neurosci. Lett.* **653**, 189–194 (2017).
19. X. F. He *et al.*, Voluntary exercise promotes glymphatic clearance of amyloid beta and reduces the activation of astrocytes and microglia in aged mice. *Front. Mol. Neurosci.* **10**, 144 (2017).
20. S. von Holstein-Rathlou, N. C. Petersen, M. Nedergaard, Voluntary running enhances glymphatic influx in awake behaving, young mice. *Neurosci. Lett.* **662**, 253 (2018).
21. Y. Meng, K. Hynynen, N. Lipsman, Applications of focused ultrasound in the brain: From thermoablation to drug delivery. *Nat. Rev. Neurol.* **17**, 7–22 (2020).
22. Z. Hu, S. Chen, Y. Yang, Y. Gong, H. Chen, An affordable and easy-to-use focused ultrasound device for noninvasive and high precision drug delivery to the mouse brain. *IEEE Trans. Biomed. Eng.* **69**, 2723–2732 (2022).
23. Z. Hu *et al.*, Targeted delivery of therapeutic agents to the mouse brain using a stereotactic-guided focused ultrasound device. *STAR Protoc.* **4**, 102132 (2023).
24. S. Chen *et al.*, A review of bioeffects induced by focused ultrasound combined with microbubbles on the neurovascular unit. *J. Cereb. Blood Flow Metab.* **42**, 3–26 (2022).
25. J. R. Lindner, Microbubbles in medical imaging: Current applications and future directions. *Nat. Rev. Drug Discov.* **3**, 527–532 (2004).
26. H. Chen, W. Kreider, A. A. Brayman, M. R. Bailey, T. J. Matula, Blood vessel deformations on microsecond time scales by ultrasonic cavitation. *Phys. Rev. Lett.* **106**, 034301 (2011).
27. H. Chen *et al.*, A new brain drug delivery strategy: Focused ultrasound-enhanced intranasal drug delivery. *PLoS One* **9**, e108880 (2014).
28. H. Chen *et al.*, Focused ultrasound-enhanced intranasal brain delivery of brain-derived neurotrophic factor. *Sci. Rep.* **6**, 28599 (2016).
29. D. Ye *et al.*, Focused ultrasound combined with microbubble-mediated intranasal delivery of gold nanoclusters to the brain. *J. Control. Release* **286**, 145–153 (2018).
30. D. Ye *et al.*, Characterization of focused ultrasound-mediated brainstem delivery of intranasally administered agents. *J. Control. Release* **328**, 276–285 (2020).
31. D. Ye, J. Yuan, Y. Yue, J. B. Rubin, H. Chen, Focused ultrasound-enhanced delivery of intranasally administered anti-programmed cell death-ligand 1 antibody to an intracranial murine glioma model. *Pharmaceutics* **13**, 190 (2021).
32. D. Ye *et al.*, Incisionless targeted adeno-associated viral vector delivery to the brain by focused ultrasound-mediated intranasal administration. *eBioMedicine* **84**, 104277 (2022).
33. J. J. Lochhead, R. G. Thorne, Intranasal delivery of biologics to the central nervous system. *Adv. Drug Deliv. Rev.* **64**, 614–628 (2012).
34. P. Hadaczek *et al.*, The "perivascular pump" driven by arterial pulsation is a powerful mechanism for the distribution of therapeutic molecules within the brain. *Mol. Ther.* **14**, 69–78 (2006).
35. J. J. Lochhead, D. J. Wolak, M. E. Pizzo, R. G. Thorne, Rapid transport within cerebral perivascular spaces underlies widespread tracer distribution in the brain after intranasal administration. *J. Cereb. Blood Flow Metab.* **35**, 371–381 (2015).
36. M. Ramos *et al.*, "Cisterna magna injection in rats to study glymphatic function" in *Methods in Molecular Biology* (Humana Press Inc., 2019), pp. 97–104.
37. C. Zhang *et al.*, Characterizing the glymphatic influx by utilizing intracisternal infusion of fluorescently conjugated cadaverine. *Life Sci.* **201**, 150–160 (2018).
38. K. Kucharz *et al.*, Post-capillary venules is the locus for transcytosis of therapeutic nanoparticles to the brain. *Nat. Commun.* **12**, 4121 (2020), 10.1101/2020.06.05.133819.
39. I. G. Gould, P. Tsai, D. Kleinfeld, A. Linninger, The capillary bed offers the largest hemodynamic resistance to the cortical blood supply. *J. Cereb. Blood Flow Metab.* **37**, 52–68 (2017).
40. Y. Meng *et al.*, Glymphatics visualization after focused ultrasound-induced blood-brain barrier opening in humans. *Ann. Neurol.* **86**, 975–980 (2019).
41. Y. Lee *et al.*, Improvement of glymphatic–lymphatic drainage of beta-amyloid by focused ultrasound in Alzheimer's disease model. *Sci. Rep.* **10**, 1–14 (2020).
42. H. Chen, A. A. Brayman, T. J. Matula, Characteristic microvessel relaxation timescales associated with ultrasound-activated microbubbles. *Appl. Phys. Lett.* **101**, 163704 (2012).
43. H. Chen, A. A. Brayman, M. R. Bailey, T. J. Matula, Blood vessel rupture by cavitation. *Urol. Res.* **38**, 321–326 (2010).
44. R. H. Kirange, R. B. Chaudhari, Utilizing mucoadhesive polymers for nasal drug delivery system. *Int. J. Pharm. Sci. Res. IJPSR* **8**, 1012–1022 (2017).
45. Y. Gong, D. Ye, C.-Y. Chien, Y. Yue, H. Chen, Comparison of sonication patterns and microbubble administration strategies for focused ultrasound-mediated large-volume drug delivery. *IEEE Trans. Biomed. Eng.* **69**, 3449–3459 (2022).
46. Z. I. Kovacsa *et al.*, Disrupting the blood-brain barrier by focused ultrasound induces sterile inflammation. *Proc. Natl. Acad. Sci. U.S.A.* **114**, E75–E84 (2017).
47. M. A. Stavarache *et al.*, Safe and stable noninvasive focal gene delivery to the mammalian brain following focused ultrasound. *J. Neurosurg.* **130**, 989–998 (2019).
48. H. Benveniste, P. M. Heerdt, M. Fontes, D. L. Rothman, N. D. Volkow, Glymphatic System Function in Relation to Anesthesia and Sleep States. *Anesth. Analg.* **128**, 747–758 (2019).
49. L. M. Hablitz *et al.*, Increased glymphatic influx is correlated with high EEG delta power and low heart rate in mice under anesthesia. *Sci. Adv.* **5**, eaav5447 (2019).
50. H. Hama *et al.*, ScaleS: An optical clearing palette for biological imaging. *Nat. Neurosci.* **18**, 1518–1529 (2015).